RESEARCH ARTICLE | OCTOBER 30 2023

High phase resolution: Probing interactions in complex interfaces with sum frequency generation FREE

Special Collection: Special Topic Collection: Tutorials in Sum-Frequency Generation Spectroscopy

Mary Jane Shultz ➡ ⑩ ; Patrick Bisson; Jing Wang; Joam Marmolejos; Rebecca G. Davies ؈ ; Emma Gubbins ⑩ ; Ziqing Xiong



Biointerphases 18, 058502 (2023) https://doi.org/10.1116/6.0002963





CrossMark



Physics of Fluids

Special Topic: K. R. Sreenivasan: A Tribute on the occasion of his 75th Birthday

Submit Today





High phase resolution: Probing interactions in complex interfaces with sum frequency generation

Cite as: Biointerphases 18, 058502 (2023); doi: 10.1116/6.0002963 Submitted: 12 July 2023 · Accepted: 20 September 2023 · Published Online: 30 October 2023







Mary Jane Shultz,^{1,a)} Datrick Bisson,² Jing Wang,^{1,b)} Joam Marmolejos,¹ Rebecca G. Davies,¹ D

AFFILIATIONS

Laboratory for Water and Surface Studies, Tufts University, Pearson Laboratory, 62 Talbot Ave., Medford, Massachusetts 02155 ²Cambridge Polymer Group, Inc., 100 Trade Center Drive, Suite 200, Woburn, Massachusetts 01801

Note: This paper is part of the Biointerphases Special Topic Collection Tutorials in Sum-Frequency Generation Spectroscopy.

- ^{a)}Author to whom correspondence should be addressed: Mary.Shultz@Tufts.edu
- b)Current address: 2 Samoset Ln., Sharon MA, 02067.

ABSTRACT

An often-quoted statement attributed to Wolfgang Pauli is that God made the bulk, but the surface was invented by the devil. Although humorous, the statement really reflects frustration in developing a detailed picture of a surface. In the last several decades, that frustration has begun to abate with numerous techniques providing clues to interactions and reactions at surfaces. Often these techniques require considerable prior knowledge. Complex mixtures on irregular or soft surfaces—complex interfaces—thus represent the last frontier. Two optical techniques: sum frequency generation (SFG) and second harmonic generation (SHG) are beginning to lift the veil on complex interfaces. Of $\frac{1}{2}$ these techniques, SFG with one excitation in the infrared has the potential to provide exquisite molecular- and moiety-specific vibrational data. This Perspective is intended both to aid newcomers in gaining traction in this field and to demonstrate the impact of high-phase resolution. It starts with a basic description of light-induced surface polarization that is at the heart of SFG. The sum frequency is generated when the input fields are sufficiently intense that the interaction is nonlinear. This nonlinearity represents a challenge for disentangling data to reveal the molecular-level picture. Three, high-phase-resolution methods that reveal interactions at the surface are described.

Published under an exclusive license by the AVS. https://doi.org/10.1116/6.0002963

I. INTRODUCTION

Surfaces play key roles in phenomena ranging from atmospheric processes to nutrient uptake in soils to heterogeneous catalytic conversions to biological processes at membranes. Understanding and manipulating these disparate processes are greatly aided with an atomic-molecular level picture of both the static configuration and interactions at the surface. Generating such a picture particularly for interfaces consisting of molecular mixtures or soft interfaces such as water is particularly challenging. Currently, there are only two techniques capable of probing such surfaces, including buried interfaces, with the atomic-molecular level specificity required to construct such a picture. These are sum frequency generation (SFG) and its electronic cousin, second harmonic generation (SHG). Both use light beams: SFG typically uses an infrared and a visible beam, and SHG uses two visible-frequency photons. Because it uses an infrared beam, SFG is a vibrational spectroscopy, thus can provide high-resolution, molecule- and moiety-specific data. This Perspective, thus, focuses on SFG, although the light-material interactions are common to both techniques.

Several overviews of SFG have been published;¹⁻⁷ this Perspective begins with a simple description of light beam-surface interactions. Weak light beams create a mild perturbation, producing familiar infrared, Raman, and UV-visible spectroscopy. More intense beams generate a stronger perturbation including secondorder responses. Thus, the advent of SFG and SHG coincided with the invention of the laser.^{8–10} One challenge in interpreting SFG or SHG output lies in this second-order perturbation: it is nonlinear. Explicitly, in linear spectroscopy, the intensity absorbed or emitted, I, from a mixture of two species, A and B, is simply the sum of that

from A (I_A) with that from B (I_B) : $I = I_A + I_B$. In nonlinear spectroscopy, the amplitudes combine. The intensity observed is proportional to the square of the combined amplitudes: $I \propto |A_A + A_B|^2$, where A_A and A_B are the respective amplitudes of A and of B. These phenomena are similar to beat frequencies and overtones in music sound waves; beats and overtones create the richness of a symphony. Here, the challenge is increased by the wrinkle that amplitude responses are not real in the mathematical sense. The real parts add and the imaginary parts add; the observed intensity is the square of this complex quantity: the vector sum squared. Note that the word complex has two meanings in this Perspective: one as a multicomponent mixture or an irregular surface, the other as containing an imaginary part. One is chemical, the other mathematical. In the mathematical sense the sum then square results in nonunique separation into contributions from the separate chemical species; separation is required for analytical measurements of surface species. Addressing the mathematical challenge, recent advances in SFG include methods for deducing the component real (Re) and imaginary (Im) amplitudes—phase-sensitive measurements. Three, high-resolution methods are described in section titled Measuring a Complex Response.

There is a reward for handling the complexity; the complex amplitudes contain rich information revealing not only surface coverage and vibrational mode orientation but also interactions. This Perspective contains three examples: an octadecylphosphonic acid (OPA) monolayer on Z-cut quartz, aqueous acetonitrile, and an octadecyltrichlorosilane (OTS) monolayer on fused silica. Results from the two monolayers show three important signatures: a resonance from the surface-attached group indicating the molecular structure of the attachment, a strong resonance from the terminal methyl group showing its orientation, and a signal from gauche defects revealing that the long chains contain kinks. Furthermore, the terminal methyl group resonances show that interactions in both packed monolayers prevent free rotation. Discussion of these examples (Secs. III A and III C) demonstrates extracting these conclusions from the experimental data. Soft interfaces include those of aqueous solutions; aqueous solutions remain an active subject of discussion. 11-13 This Perspective contains description of a self-referencing technique (Internal Reference: polarization interference) that provides insight into interactions at the aqueous interface. The conclusion is that SFG provides information beyond that provided by linear infrared, Raman, or UV-visible absorption; information that enables painting the atomicmolecular level picture referenced in the abstract.

II. SURFACE POLARIZATION

An effective perspective for imagining interaction between light with surface is that used by Feynman¹⁴ in discussing the origin of the index of refraction and birefringence. In brief, light consists of oscillating electric and magnetic fields-consider only the electric field; to a good approximation, it is an oscillating dipole. Atoms, that constitute all matter, consist of a core and surrounding electron cloud. The photon electric field interacts with this charge distribution in matter. Like running in water at the beach, this interaction has the effect of compressing the spacing between peaks of the oscillating electric field as though the beam was traveling slower, captured in a quantity called the index of refraction, n,

$$n = -\frac{c}{v},\tag{1}$$

where v is the speed in the medium and c is the speed of light in a vacuum. Some matter is isotropic, so the index of refraction is nondirectional. Other matters, particularly crystalline materials, vary in density depending on the direction. Ice is one such example: the hexagonal structure has greater density perpendicular to the hexagonal prism axis than along the axis: ice is a birefringent material. Z-cut quartz is not only birefringent, but also chiral due to the spiral structure of the silicate tetrahedra in the crystal. The chiral structure results in a nonisotropic surface. All nonlinear crystals including those used in lasers are at least birefringent. Polarization rotators are another example of using the index of refraction to impact the polarization direction.

Polarization: More technically, the impinging electric field polarizes charges in the medium. Since the light electric field oscillates, the resultant polarization, \tilde{P} , also oscillates. The oscillating polarization subsequently radiates giving rise to the emitted light. To first order, the output is merely proportional to the input light field amplitude; to second order, it is quadratic in the fields,

$$\tilde{\mathcal{P}} = \tilde{\tilde{\alpha}}^{(1)} \tilde{E}_1 + \tilde{\tilde{\alpha}}^{(1)} \tilde{E}_2 + \tilde{\tilde{\tilde{\chi}}}^{(2)} : \tilde{E}_1 \tilde{E}_2 + \cdots, \tag{2}$$

where $\tilde{\tilde{\alpha}}^{(1)}$ is a matrix describing the first-order response to the incoming field amplitude(s), \tilde{E}_i , i=1 or 2. The \sim notation indicates tensor order. This Perspective focuses on the secondorder response, $\tilde{\tilde{\chi}}^{(2)}$, termed the second-order susceptibility. Second-order susceptibility is a rank three tensor that gives rise to second-order polarization, $\tilde{\mathcal{P}}^{(2)}$,

$$\tilde{\mathcal{P}}^{(2)} = \tilde{\tilde{\chi}}^{(2)} : \tilde{E}_1 \tilde{E}_2. \tag{3}$$

If the two fields are of the same frequency, the result is SHG; if the frequencies differ, the result is either SFG or difference frequency generation (DFG). Due to symmetry, the second (and all even order) responses vanish in isotropic media; the bulk phases on either side of an interface are typically isotropic. With no signal from the bulk, the second-order polarization probes the surface without interference from the bulk.

Coupling in, coupling out: In order to polarize the medium, the electric field must couple into the medium. The efficiency with which it couples in is called a Fresnel factor, K; the efficiency with which the light generated from the polarization couples out is often referred to as a nonlinear Fresnel factor, L. Fresnel factors are determined by the continuity of the tangential components of the \tilde{E} and $\mu^{-1}\tilde{B}$ fields across the interface, continuity contained in Maxwell's equations.⁸ These optical factors are listed in Table I for the case of SFG.^{8,15–17} (The factors for SHG can be determined from those of SFG by setting $\omega_1 = \omega_2$.)

Discussion is greatly aided by defining a surface coordinate system (Fig. 1) as follows. The Z axis is perpendicular to the

	L(SF)	K
X	$-2n_{1,\mathrm{SF}}(\omega)\mathrm{cos}\eta_{\mathrm{t,SF}}$	$2n_{1,\omega}\cos\eta_{\mathrm{i},\omega}\cos\eta_{\mathrm{t},\omega}$
Y	$\overline{n_{1,\mathrm{SF}}\mathrm{cos}\eta_{t,\mathrm{SF}}+n_{2,\mathrm{SF}}\mathrm{cos}\eta_{t,\mathrm{SF}}} \ 2n_{1,\mathrm{SF}}\mathrm{cos}\eta_{r,\mathrm{SF}}$	$\frac{\overline{n_{1,\omega}\text{cos}\eta_{\text{t},\omega}+n_{2,\omega}\text{cos}\eta_{\text{i},\omega}}}{2n_{1,\omega}\text{cos}\eta_{\text{i},\omega}}$
Z	$\overline{n_{1,\mathrm{SF}}\mathrm{cos}\eta_{r,\mathrm{SF}}+n_{2,\mathrm{SF}}\mathrm{cos}\eta_{t,\mathrm{SF}}} \ 2n_{1,\mathrm{SF}}^2n_{2,\mathrm{SF}}\mathrm{cos}\eta_{r,\mathrm{SF}}$	$\frac{n_{1,\omega} \cos \eta_{i,\omega} + n_{2,\omega} \cos \eta_{t,\omega}}{2n_{1,\omega}n_{2,\omega}^2 \cos \eta_{i,\omega} \sin \eta_{t,\omega}}$
	$\overline{\left(n'_{\rm SF}\right)^2\left[n_{1,\rm SF}{\rm cos}\eta_{t,\rm SF}+n_{2,\rm SF}{\rm cos}\eta_{t,\rm SF}\right]}$	$\overline{(n'_{\omega})^2[n_{1,\omega}\mathrm{cos}\eta_{\mathrm{t},\omega}+n_{2,\omega}\mathrm{cos}\eta_{\mathrm{i},\omega}]}$

 ^{a}XZ = plane of incidence, XY = surface plane, η_{i} = incident angle, η_{t} = transmitted angle, η_{r} = reflectance angle, $n_{2,\omega}$ = refractive index of medium 2 at frequency ω , and n' = refractive index of the interfacial layer (in recent work, n' is assigned a value midway between that of the two bounding media). K_Z differs from that of Shen et al. 17 due to the application of Snell's law to assist with connection with Fresnel factors in Born and Wolf. 15

interface, often referred to as the surface normal. Light impinges on the surface at an angle measured from the normal. The light beam propagation direction and the surface normal define a plane called the input plane. The surface X axis is in the input plane such that the projection of the light propagation vector onto the surface plane is in the positive X direction. The Y coordinate is defined to result in a right-handed coordinate system. The K_X and K_Z Fresnel factors derive from Maxwell's parallel transmission factors as follows. K_X is the parallel transmission amplitude projected onto the surface X axis via the term $\cos \eta_{t,\omega}$, where t references transmission, η is the angle, and ω is the frequency. Note that the transmitted electric field is involved due to the light penetrating the medium to interact with the material there. The K_Z factor is similarly projected via $\sin \eta_{\rm t,\omega}$ and is further modified by the factor $(n_2/$ $(n')^2$ due to treatment of the interfacial layer as a thin slab between the two bounding media. The index for the interfacial layer, n', is a subject of current discussion; 18-20 often it is a good approximation to assign n' a value midway between the indices of the two bounding media.

Note that the above-mentioned Fresnel factors assume that medium 2 is isotropic, thus, described by a single index of refraction. Extension to the case of a substrate that is birefringent is straightforward, though more complex. The simpler birefringent cases consist

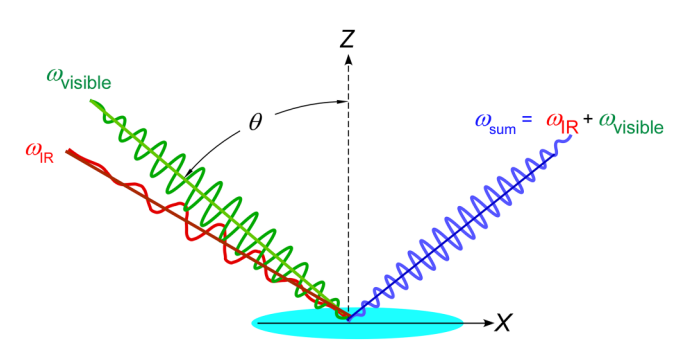


FIG. 1. Schematic of the infrared and visible input beams combining on a surface to generate the sum frequency. The input plane is defined by the surface normal (Z) and the forward beam direction along the surface (X). Beam angles are measured with respect to the surface normal.

of orienting the bulk material so that the optic axis (the c axis) is either in the input plane or perpendicular to it. If the optic axis is in the input plane and parallel to the surface, the refractive index for the X and Y components differs. If the optic axis is in the input plane but perpendicular to the surface, the refractive index for the X and Y components are the same. Quartz is a more complex material due to the chiral crystal structure. The designation "Z-cut" indicates that the optic axis is perpendicular to the surface. Handedness is indicated with a Greek α or β prefix. In this Perspective, Z-cut, α -quartz is simply referred to as Z-cut quartz.

Emitted direction: In keeping with the concept of perturbation, second-order effects are expected to be weaker than first- $\boldsymbol{\omega}$ tion, second-order effects are expected to be weaker than, e.g., Raman. order effects—SFG is expected to be weaker than, e.g., Raman. However, Raman emission is distributed over a 360° sphere. In contrast, SFG emission propagates in a well-defined direction determined by matching the tangential components of the momentum at the interface,

$$n_{1,\omega_{SF}}^{2}\omega_{SF}^{2}\sin^{2}\eta_{r,SF} = n_{1,\omega_{1}}^{2}\omega_{1}^{2}\sin^{2}\eta_{i,1} + n_{1,\omega_{2}}^{2}\omega_{2}^{2}\sin^{2}\eta_{i,2}$$

$$\pm 2n_{1,\omega_{1}}n_{1,\omega_{2}}\omega_{1}\omega_{2}\sin\eta_{i,1}\sin\eta_{i,2}\cos\delta,$$
 (4)

where SF, 1, and 2 refer to the sum frequency, input beam 1, and input beam 2, respectively, and n_{1,ω_i} is the index of refraction of the *i*th beam in the input medium, 1. The input angle η_i is measured from the surface normal as is the angle of the reflected SF beam, $\eta_{r,SF}$. The angle δ is the angle between input planes of light beams 1 and 2, respectively. In most applications, $\delta = 0$, but there are special experimental considerations in which it is convenient to have a nonzero δ . If $\delta = 0$, then Eq. (4) simplifies to

$$n_{1,SF}\omega_{SF}\sin\eta_{r,SF} = n_{1,\omega_1}\omega_1\sin\eta_{i,1} \pm n_{1,\omega_2}\omega_{SF}\sin\eta_{i,2}.$$
 (5)

The plus sign of Eqs. (4) and (5) applies if the input beams are copropagating and the minus sign if they are counterpropagating.

Beam polarization designation: It is often helpful to describe the beam electric vector, \tilde{E} , with respect to the input plane. The electric vector is always perpendicular to the propagation vector, k. The propagation vector and the surface normal define the input plane. There are two canonical directions to characterize the electric vector with respect to the input plane: either in the input



plane, designated as *p*-polarized light, or perpendicular to it, designated as *s*-polarized light.

SFG involves three beams: the sum frequency, the visible, and the infrared in order of wavelength. SFG spectra are, thus, designated according to the polarization of these three beams. The most common combinations are *ssp*—indicating *s*-polarized sum frequency, *s*-polarized visible, and *p*-polarized infrared—or *ppp*—indicating that all three beams are *p* polarized. For an isotropic surface, only *ssp*, *ppp*, and *sps* are symmetry allowed. (Except for the Fresnel factors, *pss* is the same as *sps* due to the symmetry of the Raman tensor.)

Coupled polarizations: The two impinging light beams at frequencies ω_1 and ω_2 induce a combined oscillating polarization in the medium. Combination is given by superposition of waves modulated by the medium. Modulation is encapsulated in the tensor $\tilde{\tilde{\chi}}^{(2)}$. The resonant part of $\tilde{\tilde{\chi}}^{(2)}_{Res}$ reflects the oscillating Raman polarization induced by the visible beam combined with the oscillating dipole induced by the infrared beam; these responses are strongest near resonance. A distinct advantage of analyzing polarization is that polarizations combine linearly; the resultant polarization due to resonances, q, in the medium is

$$\tilde{\tilde{\chi}}_{\text{Res}}^{(2)} = \sum_{q} \frac{A_q}{\omega_q - \omega_{\text{IR}} - i\Gamma_q},\tag{6}$$

where Γ_q is the bandwidth of the resonance and A_q is a combination of the infrared dipole and the Raman polarization averaged over all resonance orientations. If resonances form a band of states, the sum in Eq. (6) should be replaced by an integral over the density of states.

Equation (6) reflects both the power and the challenges in deducing information from the SFG response. The challenge is contained in the i in the denominator of Eq. (6): the SFG response is complex with real and imaginary components. To separate these, multiply by $1 = \frac{\omega_q - \omega_{1R} + i\Gamma_q}{\omega_q - \omega_{1R} + i\Gamma_q}$,

$$\tilde{\tilde{\chi}}_{\text{Res}}^{(2)} = \sum_{q} \frac{A_q (\omega_q - \omega_{\text{IR}})}{(\omega_q - \omega_{\text{IR}})^2 + \Gamma_q^2} + i \sum_{q} \frac{A_q \Gamma_q}{(\omega_q - \omega_{\text{IR}})^2 + \Gamma_q^2} = Re + Im,$$
(7)

and use the Euler relationship,

$$Ae^{i\varphi} = A\{\cos\varphi + i\sin\varphi\},\tag{8}$$

where φ is the phase. The key to the complex challenge lies in detecting the separate real and imaginary parts of the signal, i.e., to make a phase-sensitive measurement. Methods to meet this challenge with high-phase resolution are contained in Sec. III. The motivation for decoding the SFG response is that it reveals three informative quantities: (1) A_q —folded into A_q is the molecular orientation, (2) the resonant frequency, ω_q , that identifies the moiety and/or frequency shifts due to interactions, and (3) the state lifetime, Γ_q , that is sensitive to interactions. Revealing these molecular quantities is illustrated in the examples.

III. MEASURING A COMPLEX RESPONSE

As indicated above, complex quantities are not directly measurable. This was realized with the discovery of nonlinear effects by Bloembergen et al. in 1965²² along with recognition that harvesting all the information contained in the nonlinear response requires a phase-sensitive measurement. Practical measurement methods lagged considerably in part due to the fact that only relative phase can be measured and that relative phase is sensitive to position. Indeed, position sensitivity is exploited in the interferometric measurement of phase. The first SHG phase-sensitive measurement²⁻⁵ followed 20 years after discovery of nonlinear effects. It took another 20 years for the first SFG phase-sensitive measurements to appear.24 Today, many SFG and SHG phase-sensitive methods leverage spectral interference (schematic of one such technique is combining the sample wave with a wave genershown in Fig. 2); 25 ated from what is referred to as local oscillator, LO, in analog to radio frequency modulation and demodulation methods. Requirements on the LO are that it lacks vibrational resonances in the window of interest and generates a signal amplitude comparable to or somewhat larger than that of the sample of interest. Borrowing language from the radio frequency community, these measurements are often called One source of the lag in the measurement heterodyne SFG.² development is the above-indicated requirement for excellent positional control between calibrating the LO and swapping the calibration sample with the sample of interest. To appreciate the spatial accuracy required, consider that the sum frequency signal is in the visible part of the spectrum. A phase shift of 360° corresponds to a position change of a few hundred nm. Furthermore, the Euler relationship, Eq. (8), shows that the real and imaginary parts of the response are separated by a mere 90°. For a $\lambda \sim 400$ nm signal, $\lambda/4$ is on the order of 100 nm. Thus, improving phase reproducibility and accuracy is among the current directions in heterodyne measurements with the best being about $\pm 30^{\circ}$.

This Perspective presents three alternate routes to high-phase resolution measurements. Two methods generate the reference signal from the *same* interface as that of the sample, thus ensuring that the sample-reference physical separation is zero—extremely high-phase resolution. The third method uses a nonlinear interferometer. ^{43–46} Interferometers are often used to produce exquisite phase sensitivity—e.g., the laser interferometer gravitational wave observatory (LIGO) that measures phase shifts as small as 10^{-18} m—three orders of magnitude smaller than the diameter of the hydrogen nucleus! ^{47,48} Such accuracy is achieved in part due to the km long interferometer arms. The interferometer described here is laboratory scale, easily incorporated into existing SFG setups. Current phase accuracy is subdegree.

A. Sample on the phase reference

One technique to ensure reproducible sample-reference positioning and concomitant high-phase accuracy is to put the sample on the phase reference. Not all phase reference materials are suitable; the sample must not alter the nonlinear response of the substrate, and the substrate must have an orientation-dependent phase response. In this example, Z-cut quartz is the reference. Z-cut quartz produces a well-known phase shift⁴⁹ due to the abovementioned hexagonal, chiral structure of the crystal. Specifying

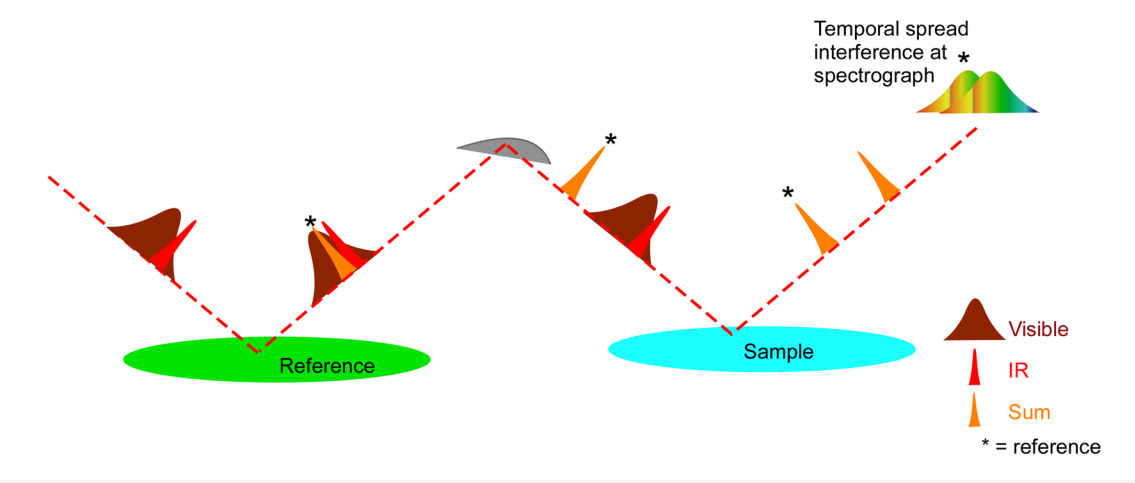
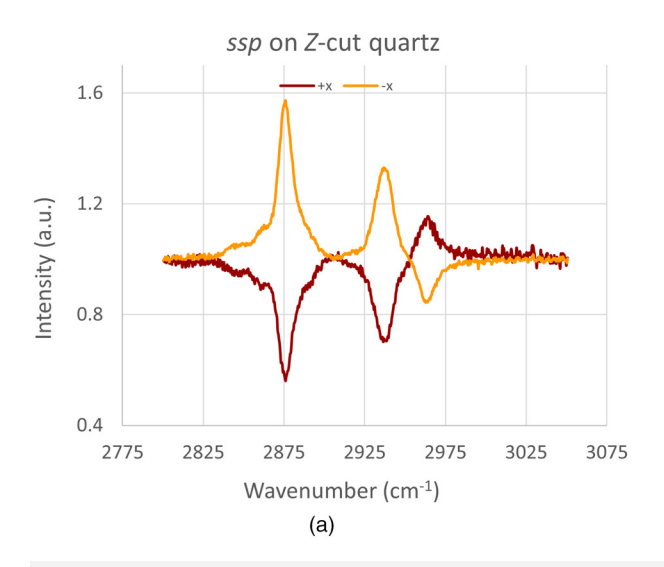


FIG. 2. Schematic of spectral interference: Time is represented by width. A sum frequency pulse is generated from a reference, also called the local oscillator (LO). The excitation beams are refocused at a sample and generate a second sum frequency pulse. Due to the short duration (50-100 fs), the reference and signal pulses travel in sequence to the grating of the spectrograph. Due to spectral dispersion in the spectrograph, both signals are temporally broadened, thus interfere. The interference is Fourier transformed, windowed, and inverse transformed to produce the spectrum.

right-handed quartz ensures that the reflected sum frequency has a -90° phase shift if the +X axis coincides with the forward direction of the reflected light. Conversely, the phase shift is $+90^{\circ}$ if the X axis oriented 180° with respect to the forward direction of the reflected light. Z-cut quartz is an excellent phase reference for many measurements since it is easily cleaned, the response originates in the bulk hence is insensitive to minor contamination,4 and has no resonances throughout the infrared. The intensity generated is comparable to, but stronger than that of water, typical hydrocarbons, amines, and other moieties of interest. A thorough discussion of Z-cut quartz can be found in Ref. 49.

Here, we examine spectra of an octadecylphosphonic acid Here, we examine spectra of an octadecylphosphonic acid (OPA) monolayer on Z-cut quartz⁵⁰ (Fig. 3, data courtesy of Hongfei Wang). The observed intensity is due to wave interference between the sample and the quartz reference; note that due to the ±90° phase shift, Z-cut quartz susceptibility is purely imaginary.

Popp on Z-cut quartz



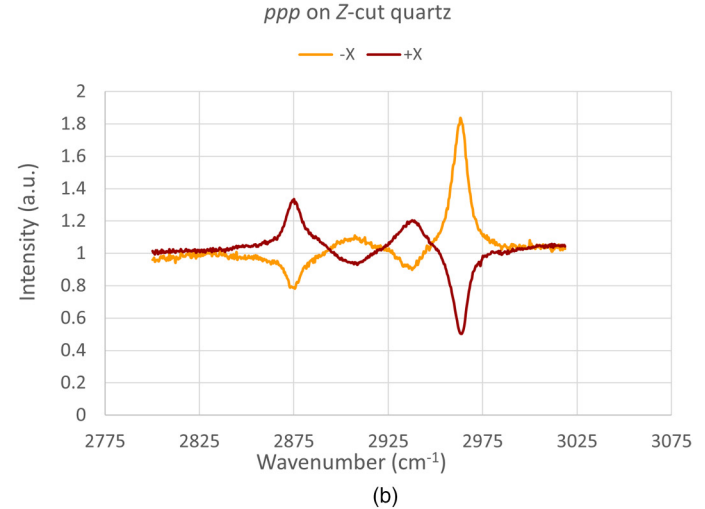


FIG. 3. SFG spectra of octadecylphosphonic acid (OPA) on Z-cut quartz. (a) With ssp polarization and Z-cut quartz oriented with the X axis in the propagation direction (brown) and with the axis oriented against the propagation direction (orange). (b) With ppp polarization and Z-cut quartz oriented with the X axis in the propagation direction (brown) and with the axis oriented against the propagation direction (orange). Note that in both cases, the +X and -X oriented spectra are near mirror images. Adapted from Fu et al., J. Phys. Chem. B 120, 1579 (2016). Not subject to U.S. Copyright. Data courtesy of Hongfei Wang.

The observed intensity is, thus,

$$I \propto |\chi_{S,Re}^{(2)} + i\chi_{S,Im}^{(2)} + i\chi_{Qtz}^{(2)}|^2 = |\chi_{S,Re}^{(2)}|^2 + |\chi_{Qtz}^{(2)}|^2 + 2\chi_{S,Im}^{(2)}\chi_{Qtz}^{(2)} + |\chi_{S,Im}^{(2)}|^2,$$
(9)

where *S* designates the sample, *Re* the real part, *Im* the imaginary part, and Qtz the *Z*-cut quartz. Normalize the intensity by dividing by the intensity of *Z*-cut quartz: $|\chi_{OIZ}^{(2)}|^2$,

$$I \propto I_{NS} + 1 + 2\chi_{NS Im}^{(2)} e^{i\varphi_{Qtz}}, \qquad (10)$$

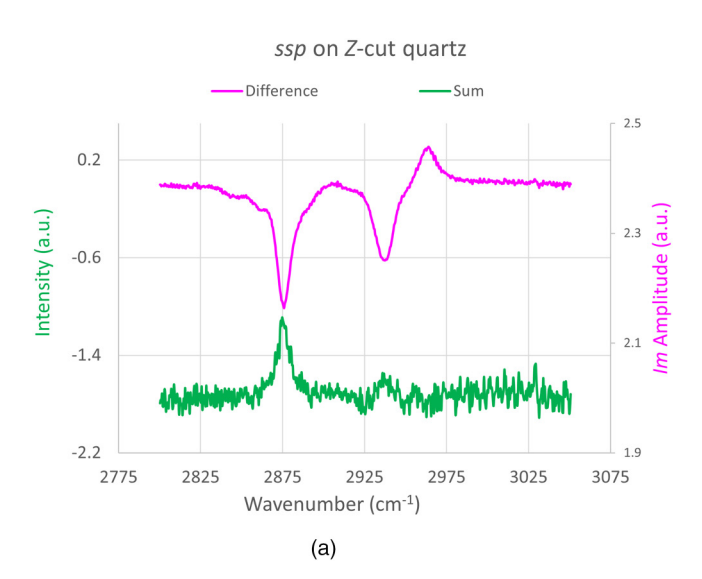
where N indicates normalized. Since $\varphi_{\rm Qtz}=\pm 90^\circ$, $e^{i\varphi_{\rm Qtz}}=\pm 1$, hence opposite signs for the last term. The spectra in Fig. 3 are not precisely mirror images due to the sample scalar intensity. Addition of the spectra reveals the sample scalar spectrum [Fig. 4(a), green trace]. The scalar spectrum is weak and, hence, shows a low signal-to-noise ratio. The imaginary part is the difference spectrum [Fig. 4(a), magenta trace]. Note that the imaginary spectrum has a much more favorable signal-to-noise ratio. The origin of the more favorable ratio is the interference: in radio frequency language, the weak monolayer spectrum is boosted from being a side band on the stronger reference carrier band. Hence, the optimal choice of a reference is one that hits the sweet spot of boosting the sample imaginary spectrum without overwhelming it. As this example shows, Z-cut quartz is often an excellent choice for monolayer samples.

The OPA spectrum also validates the phase of the *Z*-cut quartz as follows. On chemical grounds, the terminal methyl group of the long-chain hydrocarbon is oriented with the CH₃ symmetric stretch dipole (from C to H, physics definition) pointing out of the

surface. A dipole pointing out results in a negative peak as observed in Fig. 4(a), magenta trace.

Further information on the monolayer is obtained by fitting the spectrum with individual resonances (Table II). Note that the high-resolution data along with the exquisite phase resolution afforded by attaching the sample to the Z-cut quartz results in high accuracy for both resonance positions and band widths. Several features are of note:

- It is often challenging to separate antisymmetric stretch features from the Fermi resonance involving the symmetric stretch and the bend overtone. To be in resonance, the latter two must have the same symmetry, hence the same orientation. As a consequence, the amplitudes must have the same sign. Here, in *ssp*, the CH₃ *ss* has a negative amplitude, so the Fermi resonance must also be negative. The absence of the 2952.1 peak in *ppp* indicates that the 2937.20 peak is the Fermi resonance.
- The α-methylene (CH₂ attached to the surface) stretches are detectable in the *Im* spectrum despite being buried under more intense peaks in the scalar spectrum. The α-methylene features provide data about surface attachment. The larger amplitude of the *as* in *ppp* relative to *ssp* indicates that the H-C-H plane is relatively perpendicular to the surface. The stronger *ppp* as stretch relative to the *ss* is consistent with this picture.
- The methyl antisymmetric stretch is split into two peaks. The antisymmetric stretch is doubly degenerate *if* the CH₃ group freely rotates. Splitting indicates that packing prevents free rotation.
- Note that amplitudes of the *ppp* resonances are opposite to that of the corresponding *ssp* resonances. This is consistent with a



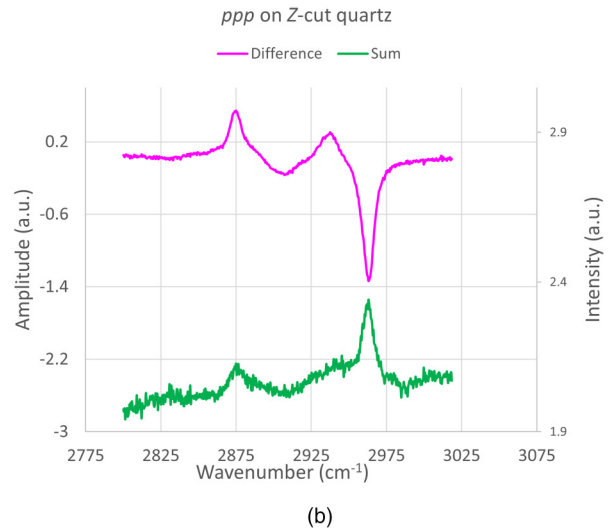


FIG. 4. Sum (green) and difference (magenta) of spectra shown in Fig. 3. The sum is the scalar spectrum, the difference is the lm part. (a) ssp of OPA on Z-cut quartz. Note that the negative resonance at $2875 \, \text{cm}^{-1}$ is primarily due to the terminal CH_3 symmetric stretch. On chemical grounds, this dipole (from C to H: physics definition of the dipole) points out of the surface, thus produces a negative peak. This validates the Z-cut quartz phase as -90° in the +X orientation. (b) ppp of OPA on Z-cut quartz. Note that the CH_3 stretch produces a positive peak due to the 180° visible phase shift on reflection.

TABLE II. Fitting parameters for imaginary spectra shown in Fig. 4.^a

	Wavenumber		A		Γ	
	ssp	PPP	ssp	PPP	ssp	ррр
Gauche	2845.9 ± 0.7	_	-0.25	_	11.8	_
Gauche	2860.1 ± 0.2	_	-0.066	_	3.0	_
CH ₃ ss	2875.7 ± 0.05	2874.8 ± 0.1	-1.27	0.74	5.08	5.6
α -CH ₂ ss	2886.7 ± 0.3	2888.0 ± 1.0	-0.14	0.08	5.2	5.2
α -CH ₂ as	<u> </u>	2906.2 ± 0.6	_	-0.64	_	12.2
Fermi	2937.20 ± 0.05	2937.1 ± 0.2	-1.13	0.64	6.56	7.5
CH ₃ as ⁺	2952.1 ± 0.7	_	-0.22	_	2.9	_
CH ₃ as-	2963.2 ± 0.1	2963.1 ± 0.03	0.58	-1.66	7.5	4.75

^aFitting parameters from Ref. 50. Assignments due to the authors.

180° phase shift of the longitudinal (Z) component of the electric field of the visible, *p*-polarized light on reflection.

The presence of gauche defects indicates that the chains do not stretch linearly.

In summary: SFG provides a detailed picture of the OPA monolayer on the Z-cut quartz surface. Interactions in the wellpacked monolayer inhibit free rotation of the terminal methyl group. The monolayer nonetheless contains many packing faults as evidenced by the signature of several gauche defects.

Spectra of OPA on Z-cut quartz demonstrate the value of a well-defined, stable phase relationship between the sample and the reference. The high spectral resolution of these data, reported at 0.3 cm⁻¹, enables self-consistent fitting of ssp and ppp data yielding accurate resonant frequencies and lifetimes. Requiring that the sample film be attached to a phase reference material, however, limits film-substrate combinations that can be probed. The next technique described is somewhat more general since it results from polarization rotation at the surface.

B. Internal reference: Polarization interference

In many systems, the quantity of interest is the orientation of the interfacial dipole measured as the angle between the surface normal and the dipole or how this orientation changes with bulk concentration. One such example is the common high performance liquid chromatography (HPLC) solvent: aqueous acetonitrile. If the orientation of interfacial acetonitrile changes with acetonitrile concentration, then interaction between a target analyte and the stationary phase-solvent would be altered, thus impacting retention times and species separation. Using such a solution would then entail time-consuming, careful calibration. Calibration simplifies if orientation is independent of concentration.

Scalar SFG studies of aqueous acetonitrile^{51–56} produced a curious result: the SFG intensity initially rose as a function of concentration as expected. However, above 7 wt. %, the signal drops. Initial interpretation of these data suggested that although the surface concentration initially increases as expected, at greater concentration, acetonitrile changes orientation.⁵⁸ Above 7 wt. %, the C≡N end group is increasingly squeezed out of the aqueous substrate and lays tangential to the surface. Randomly directed tangential dipoles net a diminished net dipole, thus diminished SFG intensity. This is a troublesome outcome for the use of aqueous acetonitrile as an HPLC solvent. An alternate explanation for the diminished intensity at higher concentration is that acetonitrile forms islands at the aqueous interface. At low concentration, molecules are isolated with the CH₃ group directed out of the surface as is expected for a hydrophobic group. As concentration increases, the strong C=N dipole adopts an antialigned configuration with neighboring acetonitrile molecules. Antialignment again reduces the orientationally averaged dipole, reducing the SFG signal without altering the dipole angle with respect to the surface $\frac{\omega}{2}$ normal; a far more favorable outcome with respect to an HPLC $\frac{\omega}{2}$ solvent.

An effective method to differentiate these alternate mechanisms for diminished intensity is to measure the net dipole orientation independent of the intensity.⁵⁸ SFG provides such a technique by leveraging polarization as follows. Light that is *s*-polarized has a dipole parallel to the surface—here labeled as tangential; ssp polarized SFG, thus, probes the tangential polarization. Light that is p-polarized is a bit more involved since a p-oriented electric field has components both parallel and perpendicular to the interface due to the input angle. Thus, ppp polarization samples four susceptibilities: χ_{XXZ} , χ_{XZX} , χ_{ZXX} , and χ_{ZZZ} . However, the Fresnel factors for χ_{XZX} and χ_{ZXX} are opposite signs, and to a good approximation, they cancel leaving a combination of χ_{XXZ} —the tangential polarization—and χ_{ZZZ} —here labeled a longitudinal polarization. Briefly, the concept is to interfere in these two polarization oscillations by rotating the input visible light polarization to 45° with respect to the input plane, hence exciting both tangential and longitudinal polarizations. The interfacial layer acts as a polarization rotator. Measuring the resultant polarization direction, thus, reveals imbalance between the tangential and longitudinal responses. The output polarization direction can be accurately determined by measuring the output intensity as a function angle for a polarizer in the output beam. Polarization is orthogonal to the null angle, so the technique is called a polarization angle null (PAN) measurement.

Combining a PAN measurement with molecular Raman depolarization data determines the spatially averaged molecular orientation. The major result for aqueous acetonitrile is that the orientation is independent of concentration-good news for HPLC. PAN data for aqueous acetonitrile are shown in Fig. 5. Notice the excellent agreement between experimental data and a $\sin^2(\text{null angle-}\theta)$ function. Convoluting the measured null angle (–9.5°) and Fresnel factors with Raman depolarization reveals that the axis of this rigid molecule is tilted $68.5^\circ\pm0.3^\circ$ from the surface normal. This is an unusually large tilt for a molecule with a hydrophobic CH $_3$ end group. Evidently, the strong interaction between the 3.6 D dipole due to the large electron density around the C=N π system and interfacial water molecules pulls the molecule fairly parallel to the interface. A deeper understanding of the mechanism leading to this configuration awaits theoretical development.

The PAN technique can be applied to any surface that is accessible to SFG so is quite versatile. It does not, however, address the nonlinear issue. For example, it cannot distinguish an inward pointing from an outward pointing dipole. For simple systems, in versus out could be predicted on chemical grounds. For more complex systems and mixtures, it is valuable to measure in versus out. In addition, nonlinearity means that smaller signals get squared into the noise, thus losing valuable information. The next technique combines the versatility of PAN with the positional accuracy of the sample on a reference technique to generate a linear response for nearly any surface that can be probed with SFG.

Acetonitrile Methyl Stretch

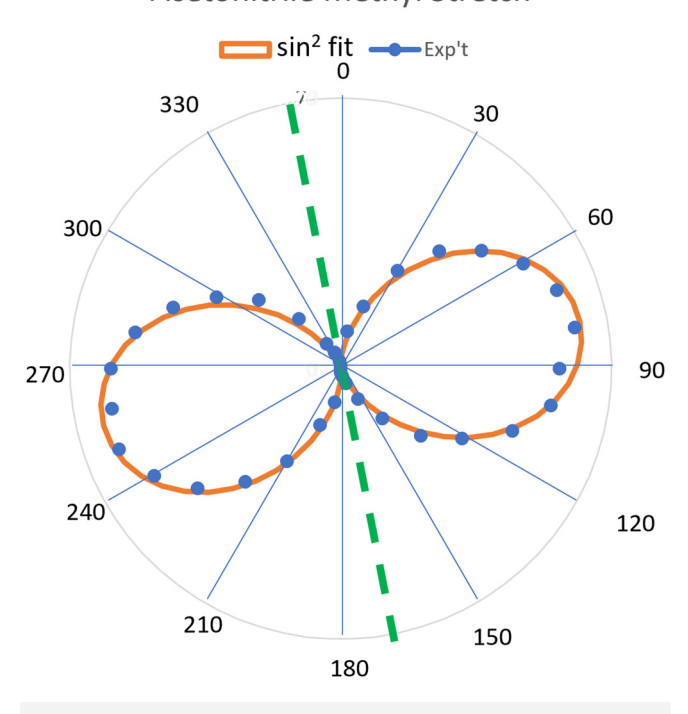


FIG. 5. PAN data of 5 wt. % aqueous acetonitrile. The emitted dipole reflects interference between the longitudinal, χ_{ZZZ} , and the transverse, χ_{XXZ} , hyperpolarizabilities. Combining with Raman depolarization data reveals the orientation; orientation is independent of concentration.

C. Nonlinear interferometer

Incorporating an interferometer, arguably the highest resolution method to detect a phase sensitive signal, is challenged by the nature of SFG: two excitation wavelengths combine to produce a third wavelength output; a nonlinear interferometer is required. Recently, this challenge has been met (Fig. 6).^{43–46} The following describes this instrument and recent results.

The nonlinear interferometer (Fig. 6) combines the power of the 180° phase shift of the sample on Z-cut quartz + X versus -X, with the versatility of separating the sample and the reference. The 180° phase shift is rigorous; it depends on conservation of energy as follows. Imagine a beam of intensity I incident on the beam splitter (BS). Part of the intensity is reflected $(r_{\rm BS})$, part transmitted $(t_{\rm BS})$: $I=(r_{\rm BS}+t_{\rm BS})I$. Each beam propagates to the beam combiner (BC) where each is again reflected $(r_{\rm BC})$ and transmitted, $t_{\rm BC}$. The intensity to ChI is

$$I_{\text{ChI}} = \left\{ r_{BS}r_{BC} + t_{BS}t_{BC} + 2\sqrt{r_{BS}r_{BC}t_{BS}t_{BC}}\cos\Delta\varphi \right\} I, \tag{11}$$

where $\Delta \varphi$ is the phase difference between the beam arriving via the sample and that arriving via the reference. Similarly, the intensity to ChII is

$$I_{\text{ChII}} = \left\{ r_{BS}t_{BC} + t_{BS}r_{BC} + 2\sqrt{r_{BS}r_{BC}t_{BS}t_{BC}}\cos(\Delta\varphi + 180^{\circ}) \right\} I \quad (12)$$

or

$$I_{\text{ChII}} = \left\{ r_{BS}t_{BC} + t_{BS}r_{BC} - 2\sqrt{r_{BS}r_{BC}t_{BS}t_{BC}}\cos(\Delta\varphi \right\} I. \tag{13}$$

Addition of Eqs. (11) and (13) gives the total output intensity: $(r_{BS}r_{BC} + t_{BS}t_{BC} + r_{BS}t_{BC} + t_{BS}r_{BC})I = \{r_{BS}(r_{BC} + t_{BC}) + t_{BS}(t_{BC} + r_{BC})\}$ I=I; conservation of light energy. The crux is the 180° phase shift $\stackrel{\rightleftharpoons}{\Rightarrow}$ in Eq. (12). A simple model for BS and BC construction producing $\frac{\aleph}{2}$ 180° reflection versus transmission phase shift is that they are made from two, face-to-face, right-angle prisms. One face is antireflection (AR) coated, and the other has a partially reflecting coat. Bring the prisms together to form a cube, orienting the prisms with the AR face on the lower prism. The beam coming into the BS cube partially reflects at the upper prism-air interface—high index to low—thus has no phase shift on reflection. The transmitted beam also has no phase shift. Similarly, at the BC, the beam originating at the reference has no phase shift on reflection to ChI. Transmitted beams have no phase shift, so neither beam to ChI has a phase shift: constructive interference. In contrast, the sample beam reflected by the BC to ChII reflects off the partially reflecting face from the air side: low index to high so it has a 180° phase shift on reflection. With a 180° phase difference, the ChII signal is destructive. (Actual construction of the BS and BC is somewhat more complex, but the essence remains.) The result is, but for path length differences, the phase of the visible beam arriving at the reference is the same as that arriving at the sample.

The visible portion of the nonlinear interferometer (A, B, C, and D) is a Mach Zehnder (M-Z) interferometer. A valuable attribute of the nonlinear interferometer is this embedded linear interferometer; it is balanced by leveraging the $\cos(\Delta\varphi)$ factor as follows. Put the same material in the sample and reference positions.

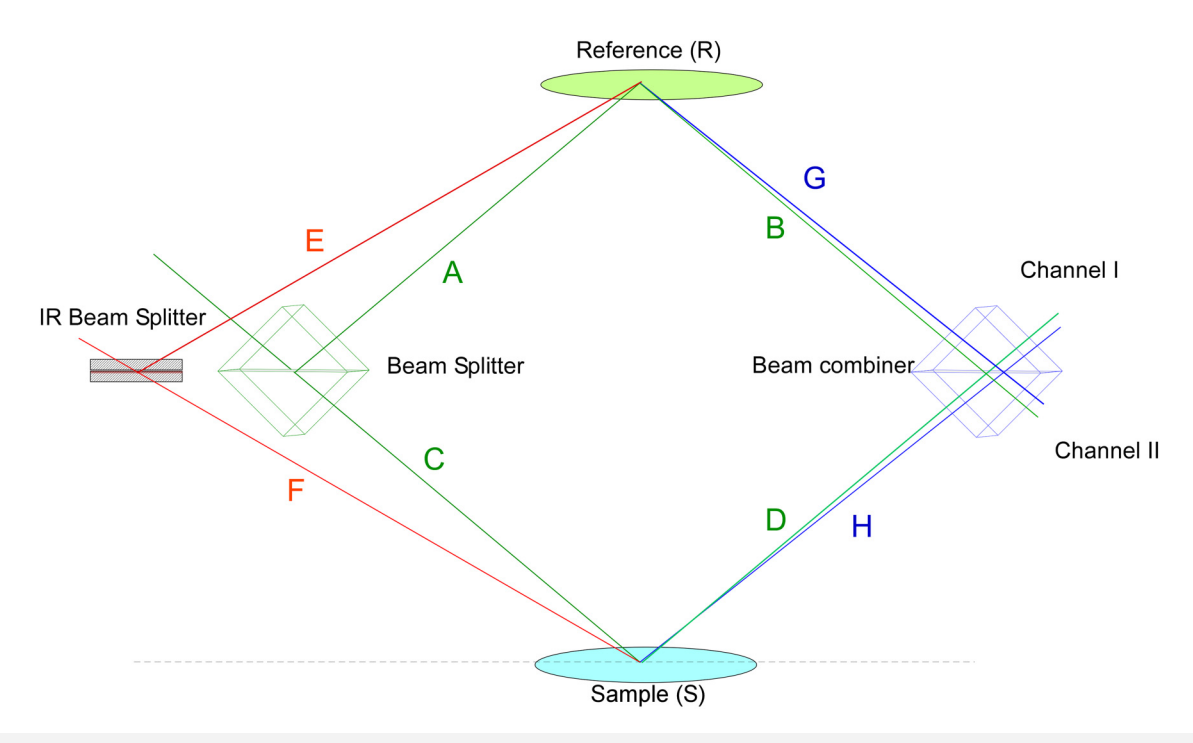


FIG. 6. Nonlinear interferometer schematic. The infrared and visible excitation beams are each split by their respective beam splitters. One visible-infrared pair excites the reference producing a reference sum frequency pulse, and the second pair excites the sample producing a sample sum frequency pulse. The sample and reference prosample producing a sample sum frequency pulse. The sample and reference prore produced. The two interferences are subsequently detected using channel I (ChI)
the same material in sample and reference positions, the Ch I signal is constructive

difference with that of the visible and infrared excitation beams. At
the splitters the reflected transmitted phase difference is gare. duced pulses combine at the beam combiner where two complimentary interferences are produced. The two interferences are subsequently detected using channel I (ChI) and a channel II (ChII) detectors. Letters A-H refer to path lengths. When aligned, with the same material in sample and reference positions, the Ch I signal is constructive and ChII is destructive.

The phase difference between the sample and reference beams on arriving at the BC is directly related to the propagation path length difference.

$$\Delta \varphi = (C + D - A - B) \times \left(\frac{2\pi}{\lambda}\right).$$
 (14)

The phase difference is zero if the upper path (A + B) is the same length as the lower (C+D) to an integral number of wavelengths. Injecting white-light into the interferometer and locating the center white-light interference ensures that the path lengths are equal to a common multiple of all white-light wavelengths, i.e., they are equal. Upon swapping a calibration sample for the sample of interest, returning to white-light balance ensures replicating the calibration sample position to this same white-light precision. There is another valuable fringe benefit to this embedded M-Z interferometer. Inject a monochromatic, e.g., HeNe beam. Since the paths are the same length for all colors, ChI is constructive and ChII is destructive for the HeNe. Use this interference to actively stabilize the M-Z interferometer, ensuring phase stabilization for the long term: weeks have been demonstrated.45

The true power of the *nonlinear* interferometer is revealed by connecting the sample and reference nonlinear signal phase the splitters, the reflected-transmitted phase difference is zero. The generated SF phase difference (in radians) is, thus,

$$\Delta_{SF}(\lambda) = \varphi_{vis}^{o}(vis\ BS) + \frac{2\pi C}{\lambda_{vis}} + \varphi_{IR}^{o}(IR\ BS) + \frac{2\pi F}{\lambda_{IR}} + \frac{2\pi D}{\lambda_{SF}} - \varphi_{vis}^{o}(vis\ BS) - \frac{2\pi A}{\lambda_{vis}} - \varphi_{IR}^{o}(IR\ BS) - \frac{2\pi E}{\lambda_{IR}} - \frac{2\pi B}{\lambda_{SF}}, \quad (15)$$

where λ is the wavelength of the corresponding beam, E and F reference the infrared paths, and G and H reference the SF beam paths. This simplifies to

$$\Delta_{SF}(\lambda) = \frac{2\pi(C-A)}{\lambda_{vis}} + \frac{2\pi(F-E)}{\lambda_{IR}} + \frac{2\pi(D-B)}{\lambda_{SF}}.$$
 (16)

Balancing the nonlinear interferometer is, hence, analogous to white-light in the linear interferometer: with a nonresonant material in sample and reference positions, the SF phase is made constant across the spectrum as follows. Neither the path lengths nor the wavelength of the visible excitation change as the frequency is tuned. Since sample and reference are identical, the phase difference is zero. To make the SF phase difference across the spectrum—at the blue

and red ends (and all wavelengths in between)-equal to zero,

$$0 = \Delta_{SF}(blue) - \Delta_{SF}(red)$$

$$= -\frac{2\pi(D-B)}{\lambda_{SF}red} = \frac{2\pi(F-E)}{\lambda_{IR}blue} + \frac{2\pi(D-B)}{\lambda_{SF}blue} - \frac{2\pi(F-E)}{\lambda_{IR}red}.$$
(17)

Hence,

$$(F - E) = (D - B) \frac{\frac{1}{\lambda_{SFred}} - \frac{1}{\lambda_{SFblue}}}{\frac{1}{\lambda_{IRred}} - \frac{1}{\lambda_{IRblue}}}$$
$$= (D - B) \frac{\{\omega_{IRblue} + \omega_{vis} - \omega_{IRred} - \omega_{vis}\}}{(\omega_{IRblue} - \omega_{IRred})} = (D - B). \quad (18)$$

So, when balanced, the IR path-length difference compensates for any SF path-length difference.

The nonlinear interferometer phase shift is tapped not only for path-length balancing, but also for shifting the sample-reference phase difference. As shown in Eq. (15), if the infrared and SF path lengths balance, then the sum frequency phase difference is directly related to the visible excitation phase difference. If this visible phase difference is zero, and Z-cut quartz is the reference adding a –90° phase shift to the reference, the signal to ChI is

$$I_{\text{ChI}} = 1 + E_{NS}^2 + 2E_{NS}\sin\delta_S,\tag{19}$$

where E_{NS} is the sample amplitude divided by that of the reference

and δ_S is the sample phase shift. The signal to ChII is

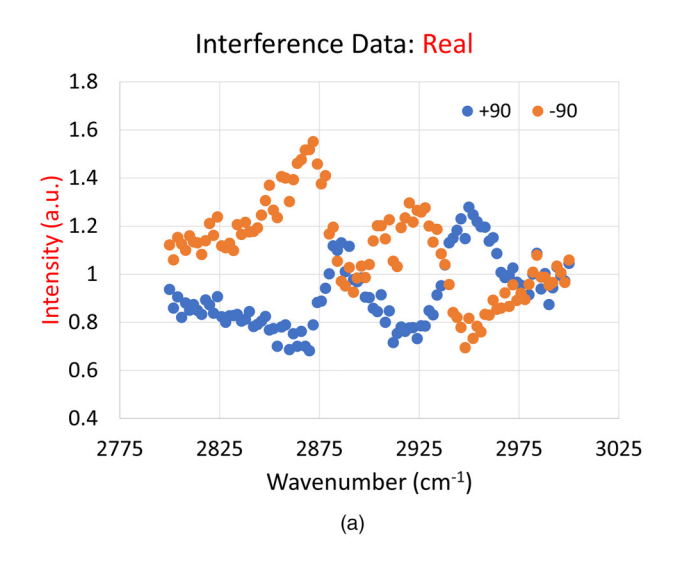
$$I_{\text{ChII}} = 1 + E_{NS}^2 - 2E_{NS}\sin\delta_S. \tag{20}$$

Similar to the sample on the Z-cut quartz, the 180° phase shift of ChII relative to that of ChI enables recovery of the sample scalar via addition of the ChI and ChII signals. The Im spectrum is obtained via subtraction.

The nonlinear interferometer provides another valuable ability: detection of the Re part. Although the Im and Re spectra are related up to an integration constant by a Cauchy transform, any non-resonant real part is masked in the transform constant. In contrast, if the visible phase is shifted 90°, the $\sin\delta_S$ in Eqs. (19) and (20) becomes $\cos\delta_S$ directly measuring the Re part, thus detecting the nonresonant as well as the resonant signal. The ability to shift the visible phase has an additional benefit: a phase-sensitive measurement can be done with a single detection channel by making two measurements separated by a 180° visible phase shift. The imaginary part is measured by combining 0° and 180° phase shift date. The real part is detected with measurements at +90° and at -90° .

An example: A monolayer of the hydrophobic coating, octade-cyltrichlorosilane (OTS), was self-assembled on fused silica according to standard procedures. ⁵⁹ It should be noted that spectra of this coating on fused silica in the literature vary somewhat from report to report. ^{55,59-63} All have two prominent peaks: one around 2875 cm⁻¹ and the other around 2940 cm⁻¹. The relative intensity of these two features varies depending on the amount of moisture in the film. Care should be exercised to ensure that all spectra are gathered from films with similar moisture content.





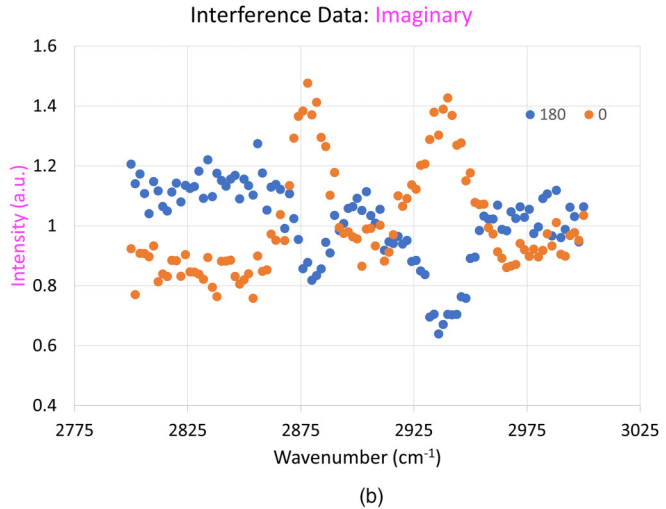
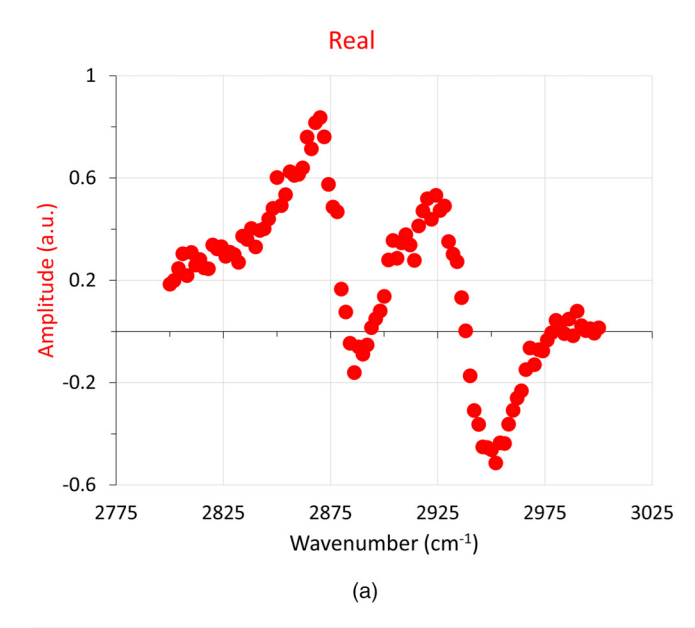


FIG. 7. Real and imaginary parts of the spectrum can be obtained by either of the two methods. (a) The real part: (single channel) Set interferometer phase to +90° and -90°, subtract the -90° spectrum from that of +90°, or (dual channel) subtract the ChII signal from that of ChI. (b) The imaginary part: (single channel) Set the instrument phase to -180° and 0°, subtract 0° from 180°, or subtract the ChII signal from that of ChI.



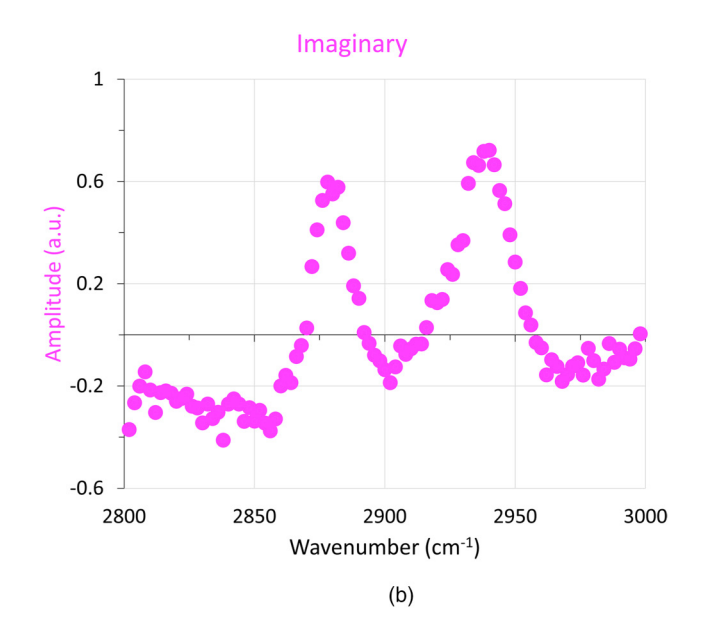


FIG. 8. Real and imaginary parts of the spectrum are obtained by (a) setting the interferometer phase to +90° and -90° and subtracting the -90° spectrum from that of +90°. (b) Set the instrument phase to -180° and 0° and subtract 0° from 180°.

Figure 7 contains the data from OTS using the single channel method. Notice the complementarity of the +90°/-90° [Fig. 7(a)] spectra as well as the +180°/0° [Fig. 7(b)] pair. The +180°/0° pair is similar to the sample on Z-cut quartz + X and -X orientation. The difference spectrum is, thus, the Im part [Fig. 8(b)]. The interferometer also enables facile collection of the Re part [Fig. 8(a)].

Although the Re and Im parts are related by a Cauchy transform, there is an advantage to collect both spectra. To probe the molecular configuration in the film, the spectra are fitted with a sum of Lorentzian peaks according to Eq. (7), using resonances consistent with the chemical composition of the film (Fig. 9). For OTS, the resonances include the symmetric stretch of the terminal methyl (CH₃ ss), the symmetric stretch of the CH₂ group anchoring the chain to the surface (α-CH₂ ss), the Fermi resonance of the CH₃ ss and the symmetric component of the doubly degenerate bend overtone, the antisymmetric stretch of the α -CH₂ (α -CH₂ as), and the CH3 antisymmetric stretch (CH3 as). There may also be features from gauche defects in the long CH2 chain. If perfectly stretched, the chain CH2 groups cancel by symmetry and net no SFG signal. A resonance red of the CH₃ symmetric stretch signals such defects. Note that the CH3 as is a doubly degenerate mode if the CH₃ group spins freely on its axis; in the film, this mode splits into two resonances. Splitting indicates that CH₃ does not spin freely. Collecting both the Re and Im spectra imposes a constraint on the fit. The resonant frequency, band width, and amplitude are characteristic of the resonances, thus are independent of probe polarization. The Re part is dispersive, and the Im part is a Lorentzian, thus provide complementary views of the goodness of fit. In addition, there may be a nonresonant component to either the Re or the Im part. Fitting both reveals any nonresonant part.

Notice that, like the spectra of a film on Z-cut quartz, the Notice that, like the spectra of a film on Z-cut quartz, the scalar spectrum obtained by adding traces is noisy reflecting a weak signal. One significant advantage of a phase-sensitive measurement is that weak signals are amplified by the nonresonant reference signal due to the cross term. In the OTS film, this magnification is

OTS - ssp

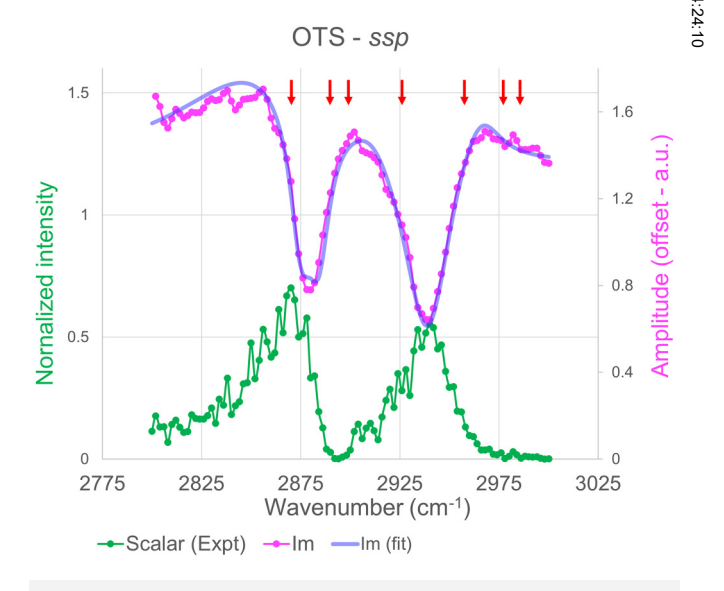


FIG. 9. Scalar (green) and Im (magenta) spectra of the OTS film. The excellent fit of the Im spectrum with resonances indicated in Table III (blue line) validates the experimental procedure and the theory.

TABLE III. OTS resonances, amplitudes, and band widths.

Resonance $\omega_{\rm q}~({\rm cm}^{-1})$	$A_{ m q}$	Γ (cm ⁻¹)	Assignment
2854	23	50	Gauche
2875	-4.5	7	CH ₃ ss
2884	-4.2	7	α -CH ₂ ss
2911	2.0	15	α -CH ₂ as
2939	-15	15	CH_3 (FR)
2966	2.4	12	$CH_2 as^+$
2956	3.5	20	CH_2 as

particularly noticeable in detecting the resonance due to the α-methylene stretch. Prior work⁶¹ could only detect these resonances by perdeutering the chain, leaving the α-CH₂ as ordinary hydrogen. Interestingly, the resonances shift slightly when the remainder of the chain consists of CD₂ groups; the α-methylene couples weakly to the remainder of the chain. In the phase-sensitive measurement, the weak α-CH₂ stretch is boosted via interference with the reference keeping coupling to the remaining chain. Detection of the α -methylene resonance is also enhanced in the phase-sensitive measurement due linearity in the interference spectrum while it is squared in the scalar spectrum.

In summary, the nonlinear interferometer technique enables phase-sensitive measurements on any interface, including buried interfaces, that are accessible to the infrared and visible beams needed to generate SFG. The Re and Im parts are measured via a simple subtraction. Measurement can be done with a single or a dual channel method. In the dual channel method, a single scan is required to produce the *Im* part, a second scan for the *Re* part.

IV. CONCLUSIONS

Generating a molecular-level picture of the surface of multicomponent mixtures or irregular surfaces such as nanoparticulate films or soft interfaces such as aqueous solutions is challenging due in part to the small numbers at the surface compared with the bulk on either side. A full monolayer consists of on the order of 1014 molecules. A comparable number in a milliliter solution corresponds to a nanomolar concentration. Thus, for most samples, the bulk signal overwhelms that on the surface. Surface molecules can interact very differently than those in the bulk-catalytic processes result in part due to this distinction. Building a molecular-level picture of an interface, thus, requires a technique that generates a signal only from the interface. Currently, the vibrational spectroscopy SFG is the only technique capable of generating a vibrational spectrum of the interface.

The surface specificity of SFG comes at a price: the generated signal is nonlinear: It is the square of an imaginary amplitude. Fortunately, the real and the imaginary parts of the signal are linear in the constituents. Advances in SFG focus on deducing these constituent amplitudes via phase-sensitive techniques. This Perspective describes three such methods.

Phase cannot be directly measured. Thus, phase-sensitive measurements interfere the signal from a sample of interest with another signal. The three techniques described here generate the interference in somewhat different ways. The first puts a sample of interest on a substrate that generates an orientation-dependent phase: Z-cut quartz in the discussed example. Z-cut quartz has a -90° phase shift on reflection if oriented with the +X axis in the propagation direction and a +90° phase shift if oriented with the -X axis in the propagation direction. The 180° shift results in spectra that are near mirror images. Addition reveals the scalar spectrum, and subtraction reveals the Im spectrum. As a fringe benefit, the nonresonant signal from the Z-cut quartz is comparable to but somewhat stronger than that of the film deposited on it. The result is that the *Im* spectrum is less noisy, thus revealing weak resonances. The Z-cut quartz results also highlight the importance of collecting two spectra with a 180° phase shift.

The second technique interferes the tangential and longitudinal polarizations by rotating the visible excitation polarization to be 45° to the input plane. The surface, thus, acts as a polarization rotator. Rotation is most sensitively detected by measuring the resultant polarization null; hence, the technique is dubbed polarization angle null (PAN). Since the surface polarization is generated by molecules in the surface, determining the degree of polarization rotation reveals the molecular orientation at the surface. The example is aqueous acetonitrile. Acetonitrile and water are completely miscible; a property that is leveraged in the use of aqueous acetonitrile in HPLC separations. Bulk miscibility does not mean that the surface consists of a weighted fraction of acetonitrile, nor that the acetonitrile molecules on the surface are randomly oriented. Attempts to determine acetonitrile surface partitioning were hampered by a signal that grew then diminished with bulk concentration. The molecular-level picture was clarified with a PAN measurement, showing that the acetonitrile orientation is constant with concentration. Coupling a PAN measurement with Paper depole. concentration. Coupling a PAN measurement with Raman depolarization data reveals that acetonitrile adopts a 68.5° tilt. This unusu- $\stackrel{\circ}{\mathbb{Z}}$ ally large tilt reflects the strong interaction between the large acetonitrile dipole and surface water molecules. The strong dipole 2 also explains the drop in signal: at bulk concentrations greater than 7 wt. %, acetonitrile molecules form islands with antialigned dipoles. Antialignment results in dipole cancelation and an accompanying drop in SFG intensity.

The third technique is a recently invented nonlinear interferometer. Interferometric techniques are well known for excellent phase sensitivity. The nonlinear interferometer uses two beam splitters sending one visible and one infrared pulse, respectively, to the sample and to the reference. The resultant sum frequency pulses propagate to a beam combiner where they interfere. Two interference signals are generated: one labeled ChI and the other ChII. The ChI and ChII signals are near mirror images just as the signals from a film on the Z cut quartz are near mirror images. The sum of the two signals is the scalar spectrum. The difference spectrum depends on the phase difference for the visible pulse at the sample and at the reference. If the phase difference is zero, the -90° phase shift of Z-cut quartz nets the imaginary (Im) spectrum. If the visible pulse phase difference is -90°, the difference is the real (Re) spectrum. Fitting the Im spectrum with a sum of Lorentzian resonances and the Re spectrum with dispersive line shapes reveals the resonant frequencies, the amplitudes (including sign), and the bandwidths or lifetimes of resonances in the surface.

Applying the nonlinear interferometer to an OTS monolayer reveals that the α -methylene group attaches to the surface with the H–C–H plane strongly longitudinal. Furthermore, the terminal CH₃ antisymmetric stretch, that is doubly degenerate if the group rotates freely has the degeneracy lifted in the film indicating chainchain interaction. A similar splitting is observed in the OPA on Z-cut quartz results.

This is an exciting time for SFG spectroscopy. Future developments with greater sensitivity are expected to yield details about surface plane distributions; one can imagine a 2D map of the surface.

ACKNOWLEDGMENTS

Partial support of this work by the United States National Science Foundation, Grant No. CHE-1807913; the United States Department of Energy, Basic Energy Sciences, Grant No. DE-SC0020258; and the United States Air Force Office of Scientific Research, Grant No. FA9550-20-1-0351, is gratefully acknowledged.

AUTHOR DECLARATIONS

Conflict of Interest

The authors have no conflicts to disclose.

Ethics Approval

Ethics approval is not required.

Author Contributions

All authors contributed equally to this work.

Mary Jane Shultz: Conceptualization (equal); Data curation (equal); Formal analysis (equal); Funding acquisition (equal); Investigation (equal); Methodology (equal); Project administration (equal); Resources (equal); Software (equal); Supervision (equal); Validation (equal); Visualization (equal); Writing - original draft (equal); Writing - review & editing (equal). Patrick Bisson: Conceptualization (equal); Formal analysis (equal); Investigation (equal); Methodology (equal); Software (equal); Validation (equal); Writing - review & editing (equal). Jing Wang: Conceptualization (equal); Investigation (equal); Methodology (equal); Validation (equal); Visualization (equal); Writing - review & editing (equal). Joam Marmolejos: Formal analysis (equal); Investigation (equal); Methodology (equal); Validation (equal); Visualization (equal); Writing - review & editing (equal). Rebecca G. Davies: Data curation (equal); Formal analysis (equal); Investigation (equal); Methodology (equal); Validation (equal); Visualization (equal); Writing - review & editing (equal). Emma Gubbins: Data curation (equal); Investigation (equal); Validation (equal); Visualization (equal); Writing - review & editing (equal). Ziqing Xiong: Data curation (equal); Investigation (equal); Methodology (equal); Validation (equal); Writing - review & editing (equal).

DATA AVAILABILITY

The data that support the findings of this study are available from the corresponding author upon reasonable request.

REFERENCES

- ¹S. M. Piontek and E. Borguet, J. Phys. Chem. C 126, 2307 (2022).
- ²S. Hosseinpour, S. J. Roeters, M. Bonn, W. Peukert, S. Woutersen, and T. Weidner, Chem. Rev. 120, 3420 (2020).
- ³H.-F. Wang, Prog. Surf. Sci. **91**, 155 (2016).
- ⁴W. Sung, D. Kim, and Y. R. Shen, Curr. Appl. Phys. 13, 619 (2013).
- ⁵S. Roke and G. Gonella, "Nonlinear light scattering and spectroscopy of particles and droplets in liquids," in *Annual Reviews of Physical Chemistry*, edited by M. Johnson and G. Cremer (Annual Reviews, Paulo Alto, CA, 2012), Vol. 63, pp. 353–378.
- ⁶Y. R. Shen and V. Ostroverkhov, Chem. Rev. 106, 1140 (2006).
- ⁷M. J. Shultz, "Sum frequency generation: An introduction plus recent developments and current issues," in *Advances in Multi-Photon Processes and Spectroscopy*, edited by S. H. Lin, A. A. Villaeys, and Y. Fujimura (World Scientific, Singapore, 2008), Vol. 18, pp. 133–200.
- ⁸N. Bloembergen and P. S. Pershan, Phys. Rev. 128, 606 (1962).
- ⁹R. K. Chang and N. Bloembergen, Phys. Rev. 144, 775 (1966).
- ¹⁰N. Bloembergen, Phys. Rev. 174, 813 (1968).
- ¹¹A. Benderskii and A. Morita, J. Chem. Phys. **151**, 150401 (2019).
- ¹²R. Kusaka, T. Ishiyama, S. Nihonyanagi, A. Morita, and T. Tahara, Phys. Chem. Chem. Phys. 20, 3002 (2018).
- ¹³Y. Otsuki, T. Sugimoto, T. Ishiyama, A. Morita, K. Watanabe, and Y. Matsumoto, Phys. Rev. B 96, 115405 (2017).
- ¹⁴R. Feynman, M. Sands, and R. B. Leighton, *Lectures on Physics* (Addison Wesley, Reading, MA, 1965).
- 15M. Born and E. Wolf, Principles of Optics: Electromagnetic Theory of Propagation, Interference and Diffraction of Light, 7th expanded (Cambridge University, Cambridge, 1999), pp. 38–48.
- ¹⁶Y. R. Shen, Ann. Rev. Phys. Chem. **40**, 327 (1989).
- 17X. Wei, S.-C. Hong, X. Zhuang, T. Goto, and Y. R. Shen, Phys. Rev. E 62, 5160 (2000)
- 18Y. R. Shen, Second Harmonic and Sum-Frequency Spectroscopy: Basics and Applications (World Scientific, Singapore, 2023).
- 19X. Yu, K.-Y. Chiang, C.-C. Yu, M. Bonn, and Y. Nagata, J. Chem. Phys. 158, 2044701 (2023).
- ²⁰C.-C. Yu, T. Seki, K.-Y. Chiang, F. Tang, S. Sun, M. Bonn, and Y. Nagata, J. Phys. Chem. B **126**, 6113 (2022).
- E. Hecht, *Optics*, 5rd ed. (Pearson, Upper Saddle River, N.J., 2015), p. 720.
- ²²R. K. Chang, J. Ducuing, and N. Bloembergen, Phys. Rev. Lett. 15, 6 (1965).
- ²³K. Kemnitz, K. Bhattacharyya, J. M. Hicks, G. R. Pinto, K. B. Eisenthal, and T. F. Heinz, Chem. Phys. Lett. **131**, 285 (1986).
- ²⁴N. Ji, V. Ostroverkhov, C.-Y. Chen, and Y.-R. Shen, J. Am. Chem. Soc. 129, 10056 (2007).
- ²⁵I. V. Stiopkin, H. D. Jayathilake, A. N. Bordenyuk, and A. V Benderskii, J. Am. Chem. Soc. 130, 2271 (2008).
- ²⁶S. Yamaguchi and T. Tahara, J. Chem. Phys. 129, 101102 (2008), 1–4.
- ²⁷W. Hua, A. M. Jubb, and H. C. Allen, J. Phys. Chem. Lett. 2, 2515 (2011).
- ²⁸M. Okuno and T. Ishibashi, J. Phys. Chem. Lett. 5, 2874 (2014).
- ²⁹ A. L. Mifflin et al., J. Phys. Chem. A 119, 1292 (2015).
- ³⁰H. Vanselous and P. B. Petersen, J. Phys. Chem. C **120**, 8175 (2016).
- ³¹N. Takeshita, M. Okuno, and T. Ishibash, J. Phys. Chem. C **121**, 25206 (2017).
- 32H. Wang, T. Gao, and W. Xiong, ACS Photonics 4, 1839 (2017).
- 33Y. Li, B. Xiang, and W. Xiong, J. Chem. Phys. 150, 114706 (2019).
- 34Y. Nojima and S. Yamaguchi, J. Phys. Chem. C 125, 23483 (2021).
- ³⁵N. Mirzajani, C. L. Keenan, S. R. Melton, and S. B. King, Opt. Express **30**, 39162 (2022)
- ³⁶P. A. Covert, W. R. Fitzgerald, and D. K. Hore, J. Chem. Phys. 137, 1 (2012).
- ³⁷B. Zelent, N. V. Nucci, and J. M. Vanderkooi, J. Phys. Chem. A **108**, 11141
- 38X. Chen, W. Hua, Z. Huang, and H. Allen, J. Am. Chem. Soc. 132, 11336 (2010).

- 39 A. G. F. de Beer, J.-S. Samson, W. Hua, Z. Huang, X. Chen, H. C. Allen, and S. Roke, J. Chem. Phys. **135**, 224701 (2011).

 40 S. E. Sanders, A. M. Stingel, and P. B. Petersen, J. Phys. Chem. Lett. **13**, 2072
- (2022)
- ⁴¹S. E. Sanders and P. B. Petersen, J. Chem. Phys. **150**, 204708 (2019).
- ⁴²S. Nihonyanagi, S. Yamaguchi, and T. Tahara, J. Chem. Phys. 130, 204704
- ⁴³J. Marmolejos, P. J. Bisson, and M. J. Shultz, J. Chem. Phys. 150, 124705 (2019), 1-8.
- ⁴⁴J. Wang, P. J. Bisson, J. M. Marmolejos, and M. J. Shultz, J. Chem. Phys. 147, 064201 (2017), 1-8, 2017 JCP Editors' Choice innovative and influential article
- ⁴⁵J. Wang, P. Bisson, J. M. Marmolejos, and M. J. Shultz, J. Phys. Chem. Lett. 7, 1945 (2016).
- ⁴⁶S. Sun, P. J. Bisson, M. Bonn, M. J. Shultz, and E. H. G. Backus, J. Phys. Chem. C 123, 7266 (2019).
- ⁴⁷A. Abramovici *et al.*, Science **256**, 325 (1992).
- 48 J. Read, Classical Quant. Grav. 40, 135002 (2023).
- ⁴⁹X.-H. Hu, F. Wei, H. Wang, and H.-F. Wang, J. Phys. Chem. C **123**, 15071 (2019).
- 50 L. Fu, S.-L. Chen, and H.-F. Wang, J. Phys. Chem. B 120, 1579 (2016).

- ⁵¹J. Kim, K. C. Chou, and G. A. Somorjai, J. Phys. Chem. B **107**, 1592 (2003). 52 Z. Hu and J. D. Weeks, J. Phys. Chem. C 114, 10202 (2010).
- 53F. Ding, Z. Hu, Q. Zhong, L. Manfred, R. R. Gattass, M. R. Brindza, J. T. Fourkas, R. A. Walker, and J. D Weeks, J. Phys. Chem. C 114, 17651
- 54Y. Rao, N. J. Turro, and K. B. Eisenthal, J. Phys. Chem. C 113, 14384 (2009). 55M. C. Henry, L. K. Wolf, and M. C. Messmer, J. Phys. Chem. B 107, 2765
- ⁵⁶M. C. Henry, E. A. Piagessi, J. C. Zesotarski, and M. C. Messmer, Langmuir 21, 6521 (2005).
- 57M. J. Makowski, A. C. Stern, J. C. Hemminger, and D. J. Tobias, J. Phys. Chem. C 120, 17555 (2016).
- ⁵⁸M. J. Shultz, P. Bisson, H. Groenzin, and I. Li, J. Chem. Phys. **133**, 054702
- 59 Y. Liu, L. K. Wol, and M. C. Messmer, Langmuir 17, 4329 (2001).
- 60 A. Ge, Q. Peng, L. Qiao, N. R. Yepuri, T. A. Darwish, M. Matsusaki, M. Akashic, and S. Ye, Phys. Chem. Chem. Phys. 17, 18072 (2015).
- ⁶¹S. Ye, S. Nihonyanagi, and Uosaki, Phys. Chem. Chem. Phys. 3, 3463 (2001).
- 62 C. S. Tian and Y. R. Shen, Proc. Nat. Acad. Sci. U.S.A. 106, 15148 (2009).
- 63 A. G. Lambert, D. J. Neivandt, A. M. Briggs, E. W. Usadi, and P. B. Davies, J. Phys. Chem. B 106, 10693 (2002).